

Structural color of metallic glass through picosecond laser

Yue'e Zhang(张月娥), Xing Tong(童星), Yuqiang Yan(闫玉强), Shuo Cao(曹硕), Hai-Bo Ke(柯海波), and Wei-Hua Wang(汪卫华)

Citation: Chin. Phys. B, 2024, 33 (**10**): 108104. DOI: 10.1088/1674-1056/ad7672
Journal homepage: http://cpb.iphy.ac.cn; http://iopscience.iop.org/cpb

What follows is a list of articles you may be interested in

Oxidation behavior of $Ti_{0.2}Zr_{0.2}Hf_{0.2}Nb_{0.2}Ta_{0.2}C$–$M_xC$ (M = Ti, Zr, Hf, Nb, Ta) composite ceramic at high temperature

Shuai Xu(徐帅), Tao Wang(王韬), Xingang Wang(王新刚), Lu Wu(吴璐),Zhongqiang Fang(方忠强), Fangfang Ge(葛芳芳), Xuan Meng(蒙萱),Qing Liao(廖庆), Jinchun Wei(魏金春), and Bingsheng Li(李炳生)
Chin. Phys. B, 2023, 32 (**6**): 068102. DOI: 10.1088/1674-1056/ac9a38

Photon-interactions with perovskite oxides

Hongbao Yao(姚洪宝), Er-Jia Guo(郭尔佳), Chen Ge(葛琛), Can Wang(王灿), Guozhen Yang(杨国桢), and Kuijuan Jin(金奎娟)
Chin. Phys. B, 2022, 31 (**8**): 088106. DOI: 10.1088/1674-1056/ac754c

LaGa-based bulk metallic glasses

Lin-Zhi Zhao(赵林志), Rong-Jie Xue(薛荣洁), Wei-Hua Wang(汪卫华), Hai-Yang Bai(白海洋)
Chin. Phys. B, 2017, 26 (**1**): 018106. DOI: 10.1088/1674-1056/26/1/018106

Amorphous phase formation rules in high-entropy alloys

Qiu-Wei Xing(邢秋玮), Yong Zhang(张勇)
Chin. Phys. B, 2017, 26 (**1**): 018104. DOI: 10.1088/1674-1056/26/1/018104

Generalized model for laser-induced surface structure in metallic glass

Lin-Mao Ye(叶林茂), Zhen-Wei Wu(武振伟), Kai-Xin Liu(刘凯欣), Xiu-Zhang Tang(汤秀章), Xiang-Ming Xiong (熊向明)
Chin. Phys. B, 2016, 25 (**6**): 068104. DOI: 10.1088/1674-1056/25/6/068104

RAPID COMMUNICATION

Structural color of metallic glass through picosecond laser

Yue'e Zhang(张月娥)[1,2], Xing Tong(童星)[2,†], Yuqiang Yan(闫玉强)[2], Shuo Cao(曹硕)[1], Hai-Bo Ke(柯海波)[2,‡], and Wei-Hua Wang(汪卫华)[1,2,3]

[1] *College of Physics, Liaoning University, Shenyang* 110036, *China*
[2] *Songshan Lake Materials Laboratory, Dongguan* 523808, *China*
[3] *Institute of Physics, Chinese Academy of Sciences, Beijing* 100190, *China*

(Received 24 July 2024; revised manuscript received 27 August 2024; accepted manuscript online 3 September 2024)

The alteration in surface color of metallic glasses (MGs) holds great significance in the context of microstructure design and commercial utility. It is essential to accurately describe the structures that are formed during the laser and color separation processes in order to develop practical laser coloring applications. Due to the high oxidation sensitivity of La-based metallic glass, it can broaden the color range but make it more complex. Structure coloring by laser processing on the surface of La-based metallic glass can be conducted after thermoplastic forming. It is particularly important to clarify the role of structure and composition in the surface coloring process. The aim is to study the relationship between amorphous surface structural color, surface geometry, and oxide formation by laser processing in metallic glasses. The findings revealed that the periodic structure primarily determines the surface color at laser energy densities below 1.0 J/mm^2. In contrast, the surface color predominantly depends on the proportion of oxides that are formed when energy densities exceed 1.0 J/mm^2. Consequently, this study provides a novel concept for the fundamental investigation of laser coloring and establishes a new avenue for practical application.

Keywords: metallic glass, picosecond laser, periodic structure, oxides

PACS: 81.05.Kf, 81.40.Tv, 81.16.Rf, 81.65.Mq **DOI:** 10.1088/1674-1056/ad7672

1. Introduction

Compared to the traditional chemical pigments, structural colors offer a broader range of application opportunities due to their high reflectivity, intensified saturation, and eco-friendliness. These attributes confer distinct advantages, such as simplified chemical compositions, simplified recycling processes, improved mechanical properties, resistance to aging, and a reduced environmental impact. Laser technology has emerged as a promising method for producing structural colors on metal surfaces as a result of its unique interaction with materials.[1,2] Additionally, the high precision of laser processing allows for the creation of ultra-high-resolution coatings (several micrometers) while simultaneously maintaining the integrity of untreated areas.[3,4] The underlying principle is the formation of periodic micro-nanostructures on the metal surface as a result of the interference of laser pulses with surface plasma,[5–8] which enables the precise control of surface characteristics. Laser-induced periodic surface structures (LIPSSs) are recognized as the primary source of structural colors generated by lasers.[9] LIPSSs find diverse applications in surface chemistry, where they are used to improve wettability and hydrophobicity, and in biology, where they are used to improve biocompatibility and biomimicry.[10–14] Although the complex interaction between laser and metal presents challenges in LIPSSs formation, practical applications have significantly advanced through direct laser induction.[15] By utilizing metal nanoparticles and nanotubes to adorn LIPSSs,[16] Guay *et al.* have demonstrated the creation of a broad color spectrum in precious metals through grating effects,[17] while Shi *et al.* have achieved multicolor impact on stainless steel surfaces via plasma effects.[18]

The advent of femtosecond and picosecond laser technology offers new avenues for precise control of structural colors. Femtosecond lasers are preferred for metal coloring due to their ablative properties, allowing for producing surfaces with high absorption and specific colors.[18–23] However, color production is limited by the regular structure of the underlying layer and its angle dependence.[24,25] Furthermore, the low pulse energy of femtosecond lasers necessitates a significant amount of time. In contrast, picosecond lasers with increased pulse energy provide cost efficiency and faster processing speeds.[26–28] The role of LIPSSs in metal surface coloring may be complicated by the rapid action of picosecond lasers on metal surfaces, which may induce phase transitions, rearrangement of surface chemical states, and structural changes, despite the achievement of color diversity.[29,30] Hence, it is essential to accurately describe the structures that are formed during laser and color separation processes in order to develop practical laser coloring applications.

Determining the structures and color separation that are

[†]Corresponding author. E-mail: tongxing@sslab.org.cn
[‡]Corresponding author. E-mail: kehaibo@sslab.org.cn

© 2024 Chinese Physical Society and IOP Publishing Ltd

formed during laser treatment necessitates a careful analysis of the surface microstructure and chemical composition. In contrast to conventional crystalline materials, metallic glass is a prospective material for structural colors,[31–33] characterized by its minimal defects and the absence of grain boundaries.[34–36] Moreover, its outstanding properties, including high tensile strength, exceptional hardness, and remarkable corrosion resistance, make it an ideal candidate for structural color applications. The formation of structural colors on metallic glass surfaces is a relatively straightforward process. For instance, the control of surface color in Zr-based bulk metallic glass is attributed to the specific metal oxide layer that is produced during femtosecond laser processing and nanosecond pulsed laser irradiation.[36–38] Utilizing nanosecond lasers, a variety of microscopic structures can be formed on the surface of Fe nanoparticles primarily through laser-induced enrichment of elements and mismatches with substrate wettability.[39] An understanding of the principles of structural color formation under laser action is indispensable for practical applications.

This study investigated the structure and composition of picosecond laser-induced coloring and color formation in La-based bulk metallic glass after thermoplastic forming. Due to its high oxidation sensitivity, it can broaden the range of surface colors. Therefore, the objective of our discourse is to elucidate the roles of structure and composition in the process of surface coloration. Analysis from both perspectives revealed that the structure predominantly influences surface coloration at low energy densities. Conversely, at energy densities surpassing a certain threshold, coloration is primarily controlled by the formation of surface oxides.

2. Experimental details

2.1. Picosecond laser processing

The $La_{62}Al_{14}Cu_{24}$ (at.%) amorphous alloy plates were prepared by die-casting a mixture of pure lanthanum (99.9%), aluminum (99.9%), and copper (99.9%) from Zhongnuo Advanced Material (Beijing). The inductively coupled plasma photometric emission spectrum (ICP-OES) was employed to verify composition of amorphous plates. The die casting plates (100 mm × 100 mm × 2 mm) were cut into samples (10 mm × 10 mm × 2 mm) and polished to the mirror-like surface. A picosecond pulsed laser coloration irradiated the mechanically-polished sample surface in the ambient atmosphere. We employed an all-solid-state ultraviolet pulse laser device in our investigations, which had a wavelength of 355 nm, a repetition frequency of 100 kHz–2 MHz, and a pulse width of 7 ps. The laser output power was fixed at 16 W. The laser pulses were directed onto the sample surface through an objective with a focal length of 100 mm. The surface was colorized by repositioning the objective in the 2D-plane, thus, placing the laser pulses over the surface. The final laser power on the surface was determined by adjusting the power percentage (10%–95%). The surface periodic structure was formed by applying a laser beam to horizontally scan the surface. The laser energy density (E) is calculated by power (P), scanning rate (v), and scanning period width (d) as

$$E = \frac{P}{dv}. \tag{1}$$

The laser energy density is the energy per square millimeter of the surface, with v ranging from 200 mm/s to 1000 mm/s and d fixed at 15 μm. The repetition frequency is fixed at 600 kHz, and v is 500 mm/s in this investigation. The laser scan area is set to be 10 mm × 10 mm, which is identical to the samples. The power percentage of the laser is adjusted to modify the groove depth of the grating, which corresponds to the energy absorbed by the metallic glasses.

2.2. Characterization

The colors were quantitatively evaluated by calculating the chromaticity x and y using the CIE color space, which is standardized by the international commission,[40]

$$x = \frac{X}{X+Y+Z}, \tag{2}$$

$$y = \frac{Y}{X+Y+Z}, \tag{3}$$

$$z = 1-x-y. \tag{4}$$

Here, X, Y, and Z (trichromatic stimulus values) can be determined through spectral reflectance, where λ represents the wavelength,

$$X = k\int_{300}^{800} S(\lambda)\rho(\lambda)\bar{x}(\lambda)\mathrm{d}(\lambda), \tag{5}$$

$$Y = k\int_{300}^{800} S(\lambda)\rho(\lambda)\bar{y}(\lambda)\,\mathrm{d}(\lambda), \tag{6}$$

$$Z = \int_{300}^{800} S(\lambda)\rho(\lambda)\bar{z}(\lambda)\mathrm{d}(\lambda). \tag{7}$$

A UV-vis-NIR spectrophotometer (HATACHI UH4150) with a wavelength range of 300 nm–800 nm was used to detect the reflectance spectra of different samples using an integrating-sphere method. The morphology characterizations were performed by employing the scanning electron microscopy (SEM; IT500). The height and angle were measured using laser scanning confocal microscopy (VK-X1100). The phase of the samples after the treatment was identified using a D8-ADVANCE x-ray diffractometer equipped with Cu $K\alpha$ ($\lambda = 0.25418$ nm) radiation. X-ray electron spectroscopy (XPS, Thermo Fisher ESCALAB XI+) was employed to determine the chemical compositions.

3. Results and discussion

3.1. Structure coloration

To explore the variation in surface structural color, the patterned surfaces were analyzed using a UV-vis-NIR spectrophotometer and the results were summarized using the CIE 1931 *XY* chromaticity diagram, as depicted in Fig. 1. The chromaticity diagram in Fig. 1(a) summarizes the surface colors obtained at different frequencies and energy densities, with each point representing the color of the sample under a parameter. Figure 1(b) is an amplified chrominance coordinate diagram that is derived from Fig. 1(a), which more clearly illustrates the multiple colors resulting from variations in energy density at different frequencies. Figure 1(c) presents a photograph of the corresponding samples illuminated by natural light. As the energy density increases at each frequency, a gradual shift in surface colors from cool to warm is observed.

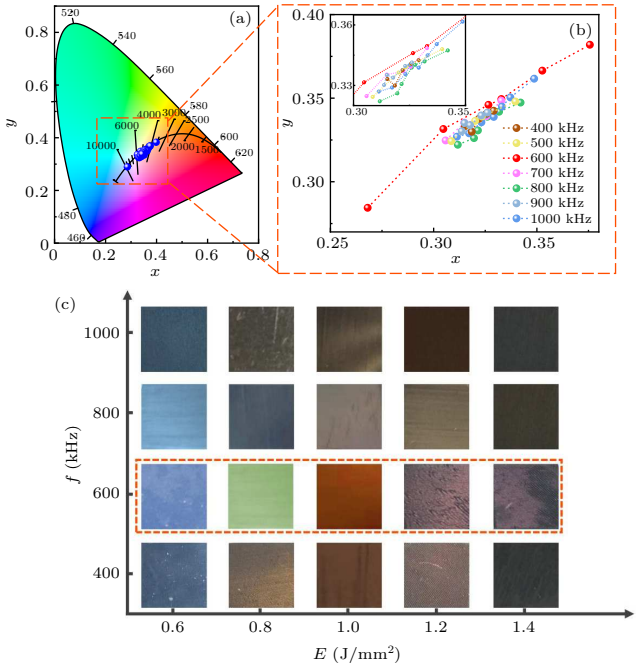


Fig. 1. The CIE *XY* chromaticity diagram. (a) The CIE 1931 of the samples prepared using a picosecond laser. (b) The enlarged image of red portion in panel (a). (c) Photographs of samples illuminated by natural light.

In particular, structural colors under 600 kHz include the color spectrum at other frequencies, which are more universal; thus, samples prepared at 600 kHz were primarily used to explore the reasons for their formation. Samples were produced with energy densities of 0.6 J/mm^2, 0.8 J/mm^2, 1.0 J/mm^2, 1.2 J/mm^2, and 1.4 J/mm^2. The red dotted box in Fig. 1(c) illustrates a gradual shift in color from cooler to warmer tones as the energy density increases. This color shift is also evident in the CIE chromaticity diagram (Fig. 2(a)), which is accompanied by the corresponding reflection spectra depicted in Fig. 2(b). In Fig. 2(b), the reflectance levels of each sample vary across different wavelengths. Specifically, each sample exhibits a high reflectivity within one wavelength band and a low reflectivity within another, which leads to the appearance of distinct observable colors. These colors correspond to peaks or valleys within the reflection spectrum. For example, the sample that was prepared with a laser energy density of 0.6 J/mm^2 displays its highest visible light absorption peak between 380 nm and 460 nm and its lowest peak between 580 nm and 700 nm, resulting in a blue-purple hue. When the energy density is increased to 0.8 J/mm^2, the highest visible light reflection peak between 460 nm and 510 nm is demonstrated as turquoise.

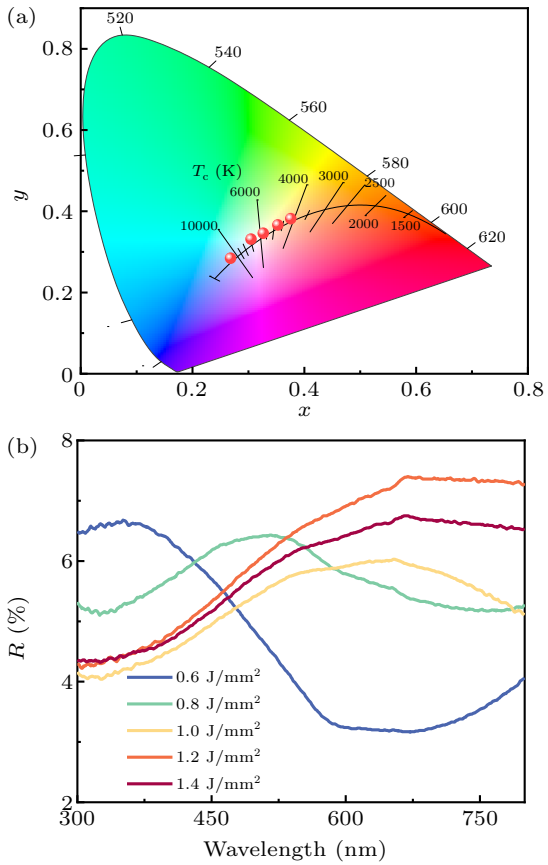


Fig. 2. (a) The CIE 1931 of the sample prepared with varying energy densities at a frequency of 600 kHz. (b) Reflection spectra corresponding to the samples in panel (a).

Conversely, the red sample prepared with an energy density of 1.0 J/mm^2 exhibits its lowest absorption peak between 350 nm and 430 nm. It is most effective at absorbing light between 670 nm and 720 nm, which corresponds to red light. This material is characterized as crimson in color, as it complements the blue-purple hues. When the energy density exceeded 1.0 J/mm^2, the reflectivity intensity gradually increased, indicating that the red color saturation gradually increased, resulting in a redder sample color. The obtained chromaticity coordinates support our earlier analysis regarding the perception of red-tone color. In addition, the stability of surface color was also studied. Reflectivity of the colored surface was measured again after exposure to atmospheric conduction for 60 days (Fig. S1). It could be found that there was almost

no change in reflectivity, indicating that the colored surfaces have good stability.

3.2. Surface morphologies

To study the impact of surface morphology on color variation, surface topographies were characterized using SEM and laser scanning confocal microscope, as depicted in Fig. 3. The matrix is polished to a mirror prior to laser action, with a flat surface and uniformly distributed elements (Fig. 3(a)). Figure S2 displays two broad haloes at 30° and 58° that are devoid of sharp crystal peaks, thereby highlighting the amorphous nature of the material before laser processing. The microstructure undergoes noticeable changes under various preparation conditions. At low magnification in the laser scanning confocal images, the surface periodic structure gradually distorts as the energy density increases. For instance, the periodic structure appears relatively smooth at 0.6 J/mm^2 (Fig. 3(b)), with micro-gratings oriented parallel to the laser radiation direction. However, the gratings no longer align parallel to the laser radiation direction as the energy density rises to 1.2 J/mm^2, as shown in high magnification SEM (Fig. 3(e-1)). This is because under picosecond laser irradiation, the temperature in the affected area of the material rises sharply, far exceeding the melting and gasification temperature of the material in a very short time, which causes the substance to undergo high ionization and form a high-temperature, high-pressure, and high-density plasma state. The inherent binding force inside the material is no longer sufficient to prevent the rapid expansion of ions and electron gases of this density, resulting in the material in the laser irradiation area erupting outward in the form of plasma. With the increase of the irradiation energy density, the plasma density increases, the energy ejected outward increases and the metal surface is more severely eroded, resulting in severe distortion and deformation of the periodic surface structure.

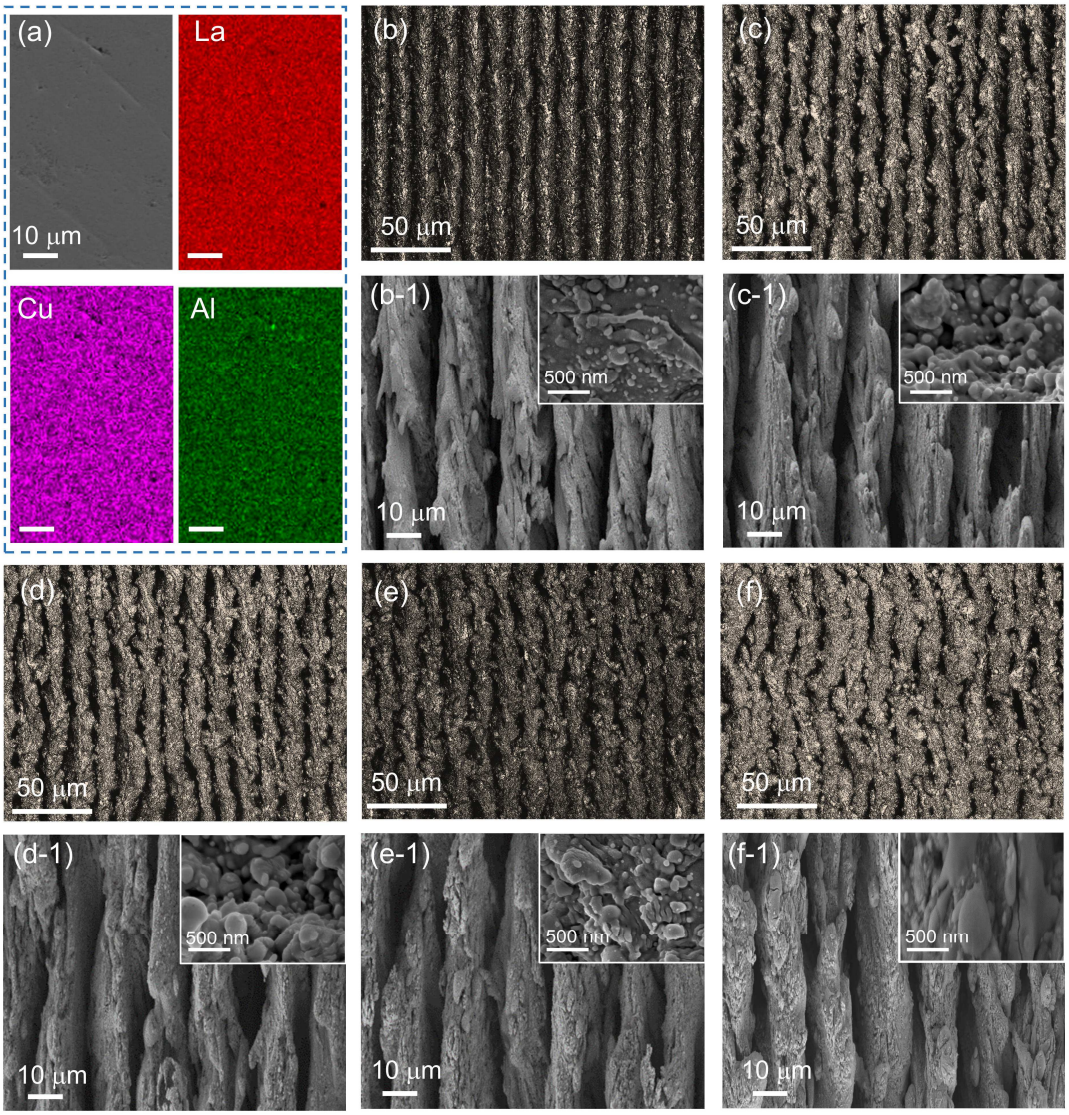


Fig. 3. Structural images of samples. (a) Surface morphology and element distribution after polishing. The low magnification microstructure by laser scanning confocal microscope and high magnification microstructure of the surface by SEM are prepared under the energy densities of 0.6 J/mm^2 (b), 0.8 J/mm^2 (c), 1.0 J/mm^2 (d), 1.2 J/mm^2 (e), and 1.4 J/mm^2 (f).

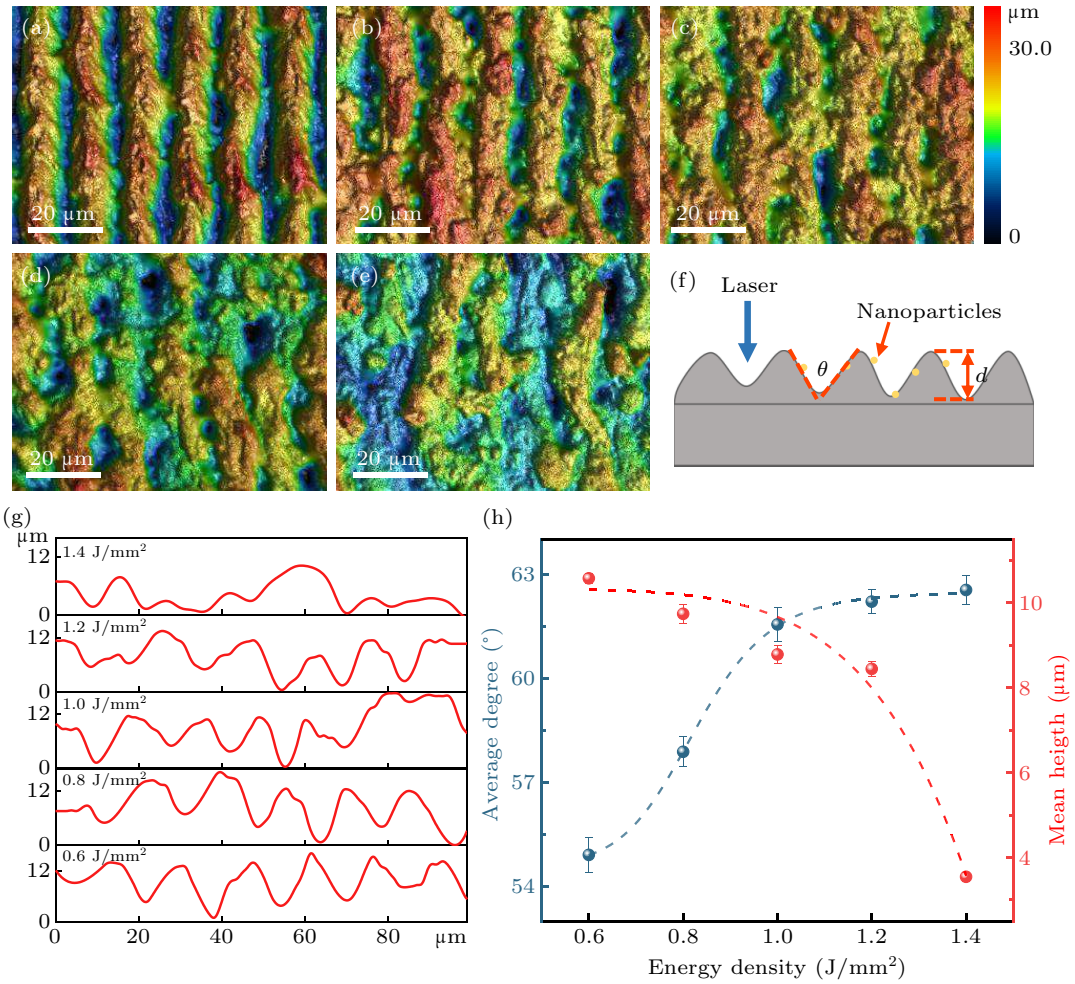


Fig. 4. The microstructure of the surface as observed through a laser scanning confocal microscope. Three-dimensional contour diagrams of samples subjected to energy densities of 0.6 J/mm^2 (a), 0.8 J/mm^2 (b), 1.0 J/mm^2 (c), 1.2 J/mm^2 (d), and 1.44 J/mm^2 (e). (f) A schematic of the morphology with randomly distributed nanoparticles. (g) Confocal cross-sectional profile diagrams of surfaces under different energy densities. (h) The average degree and mean height of the morphology with the various energy densities.

Further increase in energy density intensifies the interaction between the laser beam and the material surface, resulting in a significant increase in plasma density, which forms larger particles during rapid cooling. For example, larger droplets appear on the surface at 1.4 J/mm^2 (Fig. 3(f-1)). Although the interaction time between laser and material is short and the heat affected area is small, as the energy density increases, the amount of plasma ejected increases, and the possibility of combining in the laser processing area increases. This process, illustrated in the upper right corner of Figs. 3(b-1)–3(f-1), demonstrates that there is a corresponding increase in surface particles as the energy density increases. Nevertheless, at 1.2 J/mm^2 and 1.4 J/mm^2, a notable reduction in surface particles accompanied by intensified droplet accumulation morphology is observed. This indicates that the injected energy and plasma density are too high, causing high-temperature droplets to condense in the air and form stacks. Additionally, the energy density (Fig. S3) influences the particle diameter distribution, which initially increases and subsequently decreases as the energy density increases from 0.6 J/mm^2 to 1.2 J/mm^2. The plasma density gradually increases with increasing laser energy density, the tiny particles on the surface gradually aggregate to form larger particles, affecting the surface morphology and roughness.

To further examine the impact of the microstructure, the mean height and average degree of the microgrooves were quantitatively analyzed using a laser scanning confocal microscope, as illustrated in Fig. 4. Figures 4(a)–4(e) depict a three-dimensional scanning diagram, indicating the evolution of surface topography under different energy density conditions. This evolution reveals a more organized gully structure at a lower energy density of 0.6 J/mm^2 (Fig. 4(a)). The gully structure becomes increasingly indistinct as the energy density increases, resulting in significant morphological changes. At energy densities of 1.2 J/mm^2 and 1.4 J/mm^2, the surface is devoid of a distinct periodic structure. This observation is further supported by the sectional height depicted in the diagram (Fig. 4(g)). The sinusoidal model introduced in Fig. 4(f) is used to conduct a quantitative analysis of the impact of the surface structure. The mean height is used to

represent the average elevation from the valley base to its peak. The average degree is determined by the angle between tangential lines at the valley base, which excludes the influence of nanoparticles on the surface. To ensure the authenticity of the sample, the data obtained from five tested regions were averaged. The analysis of interface data presented in Fig. 4(g) and the graph in Fig. 4(h) illustrate the relationships between the average angle, mean height, and energy density. The mean height of the grating groove decreases from 10.5780 ± 0.121 μm at 0.6 J/mm^2 to 8.4442 ± 0.179 μm at 1.2 J/mm^2. From 0.6 J/mm^2 to 1.2 J/mm^2, the average angle increases from $55.4905° \pm 0.516°$ to $62.203° \pm 0.354°$. After applying the logistic model fitting,[41] it is found that the average degree increases rapidly below 1.0 J/mm^2 and gradually ascends to a stable value beyond 1.0 J/mm^2. The mean height decreases progressively with increasing energy density and drops sharply after surpassing 1.0 J/mm^2. These findings indicate that the mean height and average angle between two grating grooves change nonlinearly with the energy density. The interaction between the laser and the surface of samples in Fig. 4(f) produces periodic three-dimensional grating structures with varying mean heights and average angles, which significantly enhances the diffraction efficiency of Bragg in comparison to the diffraction of the materials.[42] Furthermore, the diffraction efficiency is influenced by the mean height of the grating, which is inversely proportional to the spectral bandwidth. The angle of the cone structure formed between the gratings narrows and the seemingly porous shape of the grating surface substantially improves the light trapping effect, reducing the surface reflectivity.[43] Furthermore, when it comes to the cases of 0.6 J/mm^2 and 1.4 J/mm^2, the energy density increases, resulting in a greater number of particles on the surface solidifying into larger particles and the formation of a porous flocculent morphology on the surface. This increases the roughness of the surface and reduces its density, further decreasing the refractive index and causing the reflection spectrum to shift towards a longer wavelength. The formation of surface color can be explained by the Bragg formula, assuming the surface as a sinusoidal model, wherein the grating's height is related to the spectral bandwidth[42]

$$\Delta\lambda = \frac{2nd^2 \cos\theta}{h}, \tag{8}$$

where $\Delta\lambda$ represents the spectral bandwidth, d denotes the period of the grating, n refers to the refractive index of the material, h signifies the mean height of the grating, and θ is the Bragg angle. The grating's height is greater at lower energy densities, and fewer surface particles are observed (Fig. 3), resulting in a surface color that is closer to the short-wave (blue) end of the spectrum. Conversely, as the mean height of the grating increases, the surface color shifts towards black. During this transition, the surface roughness gradually increases and the refractive index decreases, leading to a relative change in the surface's appearance.

3.3. The effect of oxides

An understanding of the internal mechanism that underpins the evolution of structural color under varying energy densities can offer valuable insights for the application of metallic glasses in structural coloration. The results indicate that the alteration in surface color is not solely due to structural differences. In the visible spectrum, the color wavelength does not linearly correlate with the energy density in either the short-wave and long-wave directions. It remains relatively unchanged once the energy density surpasses a certain threshold. Moreover, structural analyses reveal that the minimal influence extends beyond 1.0 J/mm^2. Thus, the relationship between surface composition and energy density was further explored through XRD patterns.

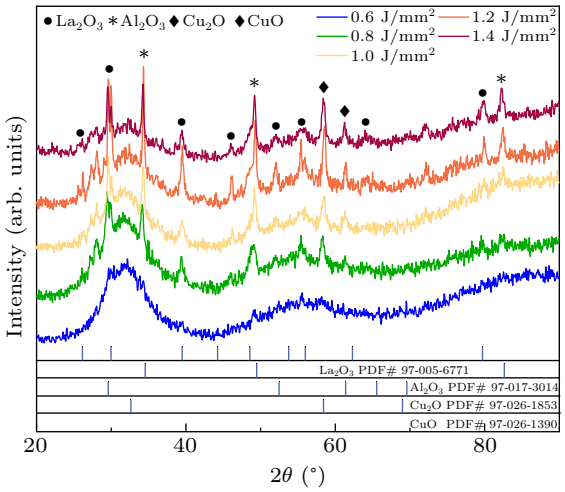


Fig. 5. XRD spectra of the laser-irradiated samples.

In Fig. 5, the XRD spectra of post-laser processing samples reveal distinct Bragg peaks, indicating modifications in their chemical compositions. Significant crystal peaks are not observed at 0.6 J/mm^2. Still, it is important to note that sharp crystal peaks corresponding to La_2O_3, Cu_2O, Al_2O_3, and CuO phases emerge on the broad hump peak under other energy densities. This suggests that oxides formed during this process also contribute to the change in surface color. It is crucial to acknowledge that the laser scans only once and has a very brief action time. This implies that the observed peaks are not the result of the overall crystallization of BMG, but rather from the crystallization behavior of the surface. In addition, the surface elements are evenly distributed without segregation (Fig. S4). As the energy density increases, so does the energy delivered by the laser to the MG surface, causing an instantaneous temperature rise that could potentially exceed 1000 °C. This process leads to the rapid oxidation of metals, especially rare earth metals, in the presence of atmospheric oxygen. Compared with other conditions, the La_2O_3 crystal

peak intensity is the most intense, while the Al_2O_3 peak intensity is the weakest at 1.0 J/mm^2. Consequently, the type and content of oxides can be modulated to produce specific structural colors by adjusting the laser power.

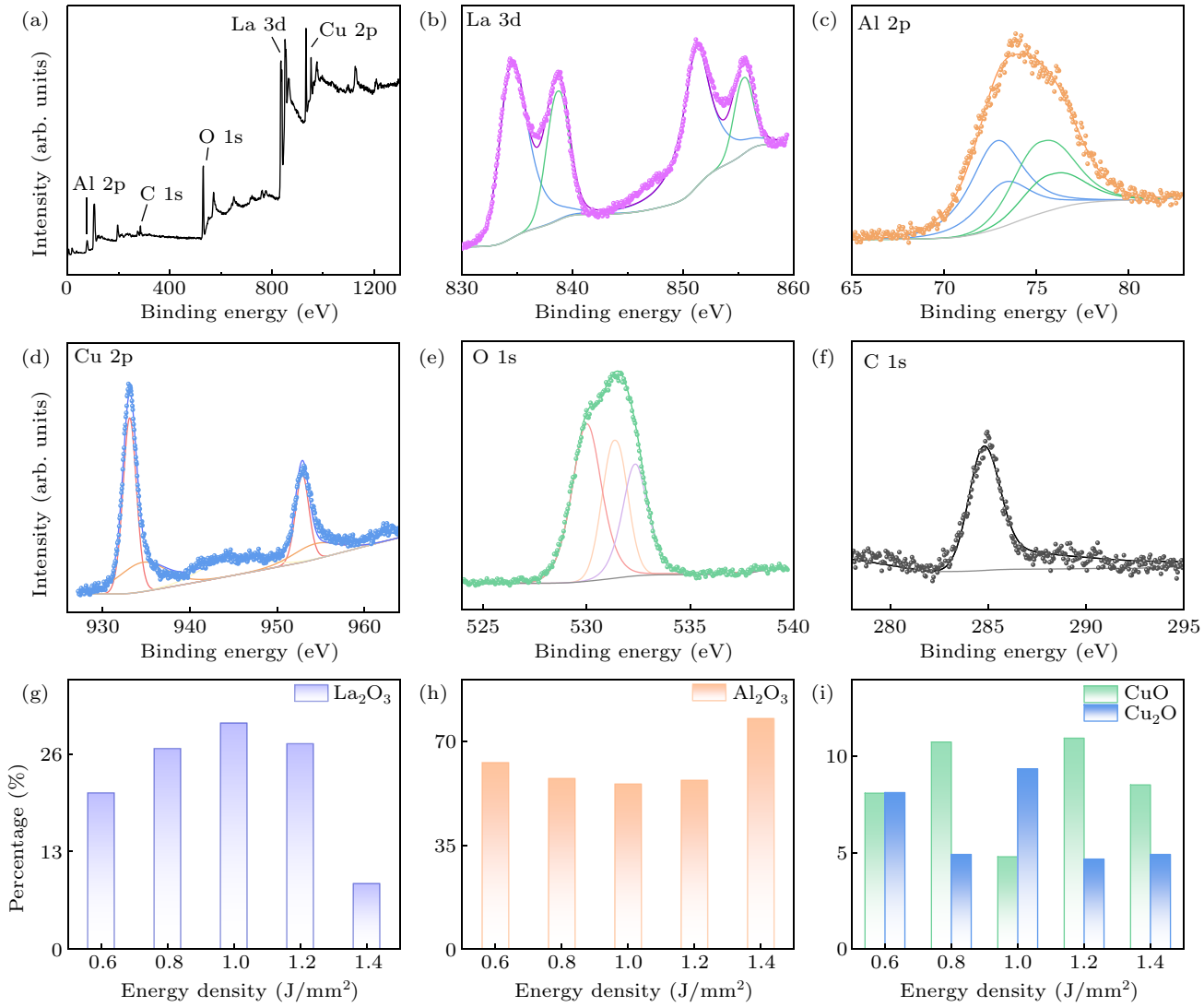


Fig. 6. XPS spectra of the samples' surface. The full spectra (a), high-resolution spectra of La 3d (b), Al 2p (b), Cu 2p (d), O 1s (e), and C 1s (f) of the sample under the condition of 0.6 J/mm^2. The doublet peaks are plotted with the same color. (g) Column diagram of La_2O_3 ratio with varying energy densities. (h) Column diagram of Al_2O_3 ratio with varying energy densities. (i) Column diagram of CuO and Cu_2O ratio with varying energy densities.

To quantitatively assess the influence of surface oxides on structural color, XPS analysis was conducted to characterize the electronic structure and surface composition of the samples, thereby enabling the calculation of component proportions. Figure 6(a) displays the full spectrum of a sample prepared at 0.6 J/mm^2, which suggests the presence of C, O, La, Al, and Cu elements on the surface. A sub-peak fit is implemented on a high-resolution map to evaluate the valence state of each element. The high-resolution La 3d spectra are deconvoluted into two doublets, which are subsequently divided by multiplet splitting (Fig. 6(b)). The presence of La^{3+} is indicated by the peaks corresponding to La 3d5 and La 3d3, which are identified at 834.42 eV and 851.07 eV, respectively. The 4.17 eV energy difference between these split peaks is consistent with the analysis indicating the presence of La_2O_3.[44,45] Although the Al can be deconvoluted into four peaks, they all correspond to Al^{3+}. The Al 2p3 peaks are located at 74.38 eV and 75.71 eV (Fig. 6(c)), which is because a part of Al is directly oxidized during the laser process, while the remaining portion is not oxidized during the laser process. This oxidation occurs on the Al in the air.[46] Furthermore, the Cu 2p spectrum exhibits five distinct peaks (Fig. 6(d)), in which the higher binding energies of Cu 2p1 and Cu 2p3 are attributed to Cu^{2+} and the lower peaks at 952.83 eV and 933.08 eV are attributed to Cu^{1+}, alongside some satellite peaks within the range of 840 eV to 847 eV.[47,48] The three peaks for O 1s in Fig. 6(e), which are located at 530.02 eV, 531.22 eV, and 532.44 eV, can be ascribed to the La–O band, Al–O, and Cu–O, respectively. In the C 1s spectrum in Fig. 6(f), the peak at 284.8 eV corresponds to the C–C band. These elements are

prone to oxidation, with oxides forming directly under laser action. The XPS spectra under alternative conditions are depicted in Fig. S5, and the peak fitting details are listed in Table S1–S5. Although the valence states of each element remained unaltered under varying energy densities, the relative content of oxides did change. According to Fig. 6(g), the proportion of La_2O_3 initially increases and subsequently decreases, with a nearly 50% reduction at 1.4 J/mm^2. However, the proportion of Al_2O_3 (Fig. 6(h)) remains nearly constant below 1 J/mm^2 and increases substantially beyond this energy density. The composition with the most notable alteration is Al_2O_3, while the change in Cu content during energy density variations is not pronounced (Fig. 6(i)). A high-pressure environment is generated during laser ablation. When the energy reaches a certain threshold, aluminum particles transfer electrons to the amorphous substrate at the interface. This high-pressure environment restricts the migration of oxygen, leading to an increase in Al_2O_3.

In summary, the influence of oxides on surface color can be quantified. When the laser energy is less than 1.0 J/mm^2, and the interaction between the laser and the material is minimal, the periodic structure on the surface becomes pronounced. The surface particles are small and hardly affect the surface structure. The composition is primarily composed of La_2O_3 and Al_2O_3, which are the result of mild oxidation. Hence, the effect on the composition is minimal, and the main coloration is determined by the periodic structure of the surface. A complete cauterization of the substances on the surface occurs as the laser energy density increases to a specific threshold level. The nanoparticles on the surface gradually merge under the influence of high temperature and pressure, forming large solidified droplets in the air, as the interaction between the laser and the substrate intensifies. This alters the surface morphology, which no longer conforms to the Bragg grating relationship. Simultaneously, the surface undergoes an increase in the formation of oxides, which obscures the surface morphology, predominantly due to the formation of various oxides in varying proportions. Therefore, when the laser energy density exceeds 1.0 J/mm^2, the surface color is predominantly influenced by oxides.

4. Conclusion

In conclusion, this analysis of the surface coloration of La-based MG blocks treated with a picosecond laser in air and its origin reveals that the laser-processed surface exhibits a diverse array of structural colors. Picosecond laser color rendition can be quantitatively defined through the periodic structure and surface oxide modulation. The periodic structure governs the capture of surface color when the energy density is below 1.0 J/mm^2, as evidenced by the surface morphology. Based on the surface chemical composition, when the energy density exceeds 1 J/mm^2, the surface color is predominantly influenced by the proportion of oxides formed. Hence, this study provides a precise control strategy for picosecond laser coloring, and this mechanism can be extended to other metal surfaces, offering guidance for picosecond laser-induced coloring and potentially advancing its practical implementation in laser coloring.

Acknowledgments

Project supported by the National Natural Science Foundation of China (Grant Nos. 52071222 and 52471180), Guangdong Major Project of Basic and Applied Basic Research, China (Grant No. 2019B030302010), Guangdong Basic and Applied Basic Research, China (Grant No. 2020B1515130007), the National Key Research and Development Program of China (Grant No. 2021YFA0716302), and the Strategic Priority Research Program of the Chinese Academy of Sciences (Grant No. XDB30000000).

References

[1] Yu H, Zhao L N, Bo M S, Xu D S and Jia L C 2023 *Rare Met.* **42** 844
[2] Liu Y N, Ding Y, Yang L J, Sun R L, Zhang T G and Yang X J 2021 *J. Manuf. Processes.* **66** 341
[3] Antończak A, Stępak B, KoziołP and Abramski K 2013 *Appl. Phys. A* **115** 1003
[4] Qi S, Jian Z Z, Xian K M, Jia N Y, Zhao H G, Ming Z and Shun G 2022 *Rare Met.* **41** 1022
[5] Hedayati K and Elbahri M 2016 *Plasmonics* **12** 1463
[6] Gu Y H, Zhang L, Yang J K, Yeo S P and Qiu C W 2015 *Nanoscale* **7** 6409
[7] Kristensen A, Yang J, Bozhevolnyi S, Link S, Nordlander P, Halas N and Mortensen N 2017 *Nat. Rev. Mater.* **2** 16088
[8] Ma Y Q, Shao J H, Zhang Y F, Lu B R, Zhang S C, Sun Y, Qu X P and Chen Y F 2015 *Chin. Phys. B* **24** 080702
[9] Camilo F, Kirner S, Krüger J and Bonse J 2020 *J. Laser Appl.* **32** 022063
[10] Florian C, Skoulas E, Puerto D, Mimidis A, Stratakis E, Solis J and Siegel J 2018 *ACS Appl. Mater. Interfaces* **10** 36564
[11] Lutey A, Gemini L, Romoli L, Lazzini G, Fuso F, Faucon M and Kling R 2018 *Sci. Rep.* **8** 10112
[12] Martínez-Calderon M, Manso-Silván M, Rodríguez A, Gómez-Aranzadi M, García-Ruiz J, Olaizola S and Martín-Palma R 2016 *Sci. Rep.* **6** 36296
[13] McDaniel C, Gladkovskaya O, Flanagan A and Rochev Y 2015 *RSC Adv.* **5** 42548
[14] Stratakisa E, Bonsec J, Heitzd J, Siegele J, Tsibidisa G and Skoulasa E 2020 *Mat. Sci. Eng. R* **141** 100562
[15] Zhi H F, Xin Y S, Peng B H, Hang F, Hui C D, Shun G, Ru S and Jian H L 2020 *Rare Met.* **39** 270
[16] Sun X D, Hui W Y, Cheng Y Z, Jing Z, Shi Y and Pan L J 2023 *Rare Met.* **42** 3304
[17] Guay J, Cala L, Cote G, Charron M, Poitras D, Ramunno L, Berini P and Weck A 2017 *Nat. Commun.* **8** 16095
[18] Shi X Y, Huang Z J, Laakso M, Niklaus F, Sliz R, Fabritius T, Somani M, Nyo T, Wang X, Zhang M, Wang G, Kömi J, Huttula M and Cao W 2019 *Appl. Surf. Sci.* **484** 655
[19] Ahmed M F, Kim Y, Lee M and Jun M 2011 *Appl. Surf. Sci.* **257** 7771
[20] Yao J W, Zhang C Y, Liu H Y, Dai Q F, Wu L J, Lan S, Gopal A, Trofimov V and Lysak T 2012 *Appl. Surf. Sci.* **258** 7625
[21] Li G Q, Li W, Hu Y L, Zhang C C, Li X H, Chu J and Huang W H 2014 *Appl. Surf. Sci.* **316** 451
[22] Ahsan M and Lee M 2013 *Optik* **124** 3631
[23] Höhm S, Herzlieb M, Rosenfeld A, Krüger J and Bonse J 2015 *Appl. Surf. Sci.* **336** 39

[24] Wang C, Lin X, Schäfer C, Hirsemann S and Ge J P 2020 *Adv. Funct. Mater.* **31** 2008601

[25] Zhou L W, Yang L L, Liu Y, Xu Z, Yin J, Ge D T and Jiang X S 2020 *Adv. Opt. Mater.* **8** 2000234

[26] Long J Y, Fan P X, Zhong M L, Zhang H J, Xie Y D and Lin C 2014 *Appl. Surf. Sci.* **311** 461

[27] Palmieri F, Ledesma R, Dennie J, Krame T, Lin Y, Hopkins J, Wohl C and Connell J 2019 *Compos. Part B-Eng.* **175** 107155

[28] Huang Y D, Zhang C Y, Zhang C C, Li G, Chen Q and Song C 2022 *J. Manuf. Processes* **76** 304

[29] Pauna H, Shi X Y, Huttula M, Kokkonen E, Li T, Luo Y, Lappalainen J, Zhang M and Cao W 2017 *Appl. Phys. Lett.* **111** 103901

[30] Xiong Y, He T T, Lu Y, Bao H S, Li Y, Ren F Z, Cao W and Volinsky A 2018 *J. Iron. Steel Res. Int.* **25** 469

[31] Wu G, Liu S D, Wang Q, Rao J, Xia W Z, Yan Y Q, Eckert J, Liu C, Ma E and Shan Z W 2023 *Nat. Commun.* **14** 3670

[32] Ashby M and Greer A 2006 *Scr. Mater.* **54** 321

[33] Chen F C, Dai F P, Yang X Y, Ruan Y and Wei B B 2020 *Chin. Phys. B* **29** 066401

[34] Bu Y, Bai X M, Lyu F C, Liu G, Wu G, Pan L L, Cheng L Z, Ho J and Lu J 2020 *Adv. Opt. Mater.* **8** 1901626

[35] Yang C, Zhang C nand Liu L 2017 *J. Alloys Compd.* **728** 289

[36] Na J, Han K, Garrett G, Launey M, Demetriou M and Johnson W 2019 *Sci. Rep.* **9** 3269

[37] Wang J Z, Zhang P L, Shen L, Yu Z S, Shi H C and Tian Y T 2021 *J. Manuf. Processes* **69** 613

[38] Hong J, Qian Y F, L Zhang, Huang H, Jiang M Q and Yan J W 2021 *Surf. Coat. Tech.* **424** 127657

[39] Qian Y F, Huang H, Jiang M Q and Yan J W 2021 *Appl. Surf. Sci.* **577** 151976

[40] Shaw M and Fairchild M 2002 *Color Res. Appl.* **27** 316

[41] Glonek G and McCullagh P 1995 *J. R. Stat. Soc.* **57** 533

[42] Ciapurin I, Drachenberg D, Smirnov V, Venus G and Glebov L 2012 *Opt. Eng.* **51** 058001

[43] Wang K X, Feng S M, Xu H T, Tian J D and Pei J 2012 *Acta Opt. Sin.* **32** 324001

[44] Yao S S, Wang Y Q, Liang Y Z, Yu H L, Majeed A, Shen X Q, Li T B and Qin S B 2021 *Ceram. Int.* **47** 27012

[45] Zhao Z H, Liu J L, Qin M, Kou K C, Wu G L and Wu H J 2020 *J. Nanosci. Nanotechnol.* **20** 3140

[46] Cañón J and Teplyakov A 2021 *Surf. Interface Anal.* **53** 475

[47] Prajapati J, Das D, Katlakunta S, Maramu N, Ranjan V and Mallick S 2021 *Inorg. Chim. Acta* **515** 120069

[48] Sudha V, Murugadoss G and Thangamuthu R 2021 *Sci. Rep.* **11** 3413